Velostat Sensor Array for Object Recognition

Liangqi Yuan, *Student Member, IEEE*, Hongwei Qu, *Member, IEEE*, and Jia Li, *Senior Member, IEEE*

***Abstract*—This paper presents a cost-effective pressure sensing system for object detection and identification. The pressure sensing system consists of a 27 × 27 piezoresistive sensor array made of carbon composite Velostat, a signal processing subsystem for signal scanning, amplification, registration, and enhancement. A convolutional neural network is used to classify various objects through the pressure signals produced and processed by the sensing array. Based on systematic characterizations and calibrations of sensing materials and system sensitivity, three experiment setups are established to recognize 10 objects to be detected. In series of experiments, a pressure image data set consisting of 32264 frames of images is first assembled to represent the 10 objects. Contrast enhancement algorithm was used to process the pressure image data set and combined with a convolutional neural network ResNet-PI to classify the 10 objects. For pressure images collected with the preestablished three experiment setups, an overall accuracy of 0.9854 is achieved. Compared with other systems based on Velostat sensor array, the system demonstrated in this study features improvements in structural robustness, detection repeatability and system reliability, suggesting its potential applications in emerging areas including human-computer interaction and smart health monitoring.**

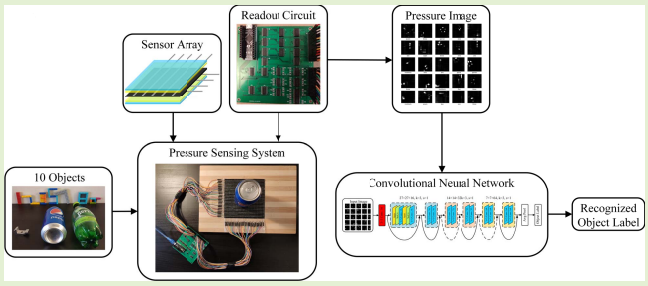

***Index Terms*—Velostat, pressure sensors, crosstalk, machine learning.**

I. Introduction

TACTILE sensing is one of the most fundamental sensing mechanisms human body develops. In the current world of human-computer interaction and intelligent health, tactile signal has widely been used as inputs for information process and control, enabling machine recognition of external excitations. The current areas where such recognition and interaction are enthusiastically pursued include, but not limited to, medical [1], [2], biological [3], [4], wearable electronics [5], [6], and robotics [7], [8]. In a particular tactile sensing system, an electrical signal is generated as a response to physical parameters such as temperature, pressure, vibration, texture, friction, etc. when the object is in close contact with the tactile sensor [1], [9]. Pressure sensors are one of the largest categories of all sensors thanks to its diverse sensing mechanisms and more importantly, easy device fabrication process thus possible low cost. Moreover, due to their miniature size enabled by semiconductor process-based microfabrication technologies, a variety of pressure sensors have been adopted in wearable electronics and medical devices where flexible sensor deployment is crucial.

Manuscript received October 22, 2021; revised November 28, 2021; accepted November 29, 2021. Date of publication December 3, 2021; date of current version January 12, 2022. The associate editor coordinating the review of this article and approving it for publication was Prof. Meribout Mahmoud. *(Corresponding author: Jia Li.)*

The authors are with the Department of Electrical and Computer Engineering, Oakland University, Rochester, MI 48309 USA (e-mail: liangqiyuan@oakland.edu; qu2@oakland.edu; li4@oakland.edu).

Digital Object Identifier 10.1109/JSEN.2021.3132793

Based on their physical responses and sensing mechanisms, pressure sensors can mainly be categorized into the following types, i.e., capacitive, piezoelectric, optical, piezoresistive [9]–[12]. Capacitive pressure sensors feature high sensitivity, low-temperature dependence, and low noise floor, which are desirable for applications with high precision and harsh environments [13]–[15]. Piezoelectric materials have found promising applications in wearable electronics thanks to their dual energy flow – can be used as both sensing and energy generating elements. In this particular area, a variety of triboelectric devices with self-powering capability have been actively attempted, despite that the fabrication process for such materials and devices are normally not compatible with standard technologies [10]. Optical pressure sensors have great attributes such as high sensitivity and outstanding interference immunities. However, their bulky system configurations hinder their applications in many areas where deployment flexibility is a concern [16], [17]. Piezoresistive pressure sensors, however, take many forms of materials and structures for large array of applications. Because of their overall easy fabrication, low-cost, simple signal processing circuitry and standard data acquisition process, piezoresistive sensors have steadily been the dominating category in pressure sensing [18], [19]. In contrary to silicon and metal based piezoresistive sensors and strain gains for process control and specific pressure monitoring, some flexible piezoresistive materials have demonstrated their great advantages in easy deployment, which is of particular important for biomedical and human-machine interacting systems.

To this end, various pressure sensor arrays based on Velostat, an elastic polymer with conductive additive with piezoresistive characteristics, have been extensively explored recently [20], [21]. Sundaram *et al.* [22] have demonstrated tactile gloves for object-grasping robotics, in which convolutional neural network (CNN) is employed to recognize the type of objects and judge the responding gestures of the robotics, through the signals provided by Velostat sensors integrated in the gloves. Chen *et al.* [23], [24] have developed pressure sensor insoles to assist inertial measurement unit (IMU) for indoor human positioning. Hudec *et al.* [25] have utilized Velostat pressure sensors in their mattress designed to detect the position of the lying person to prevent bedsores. Hopkins *et al.* [26] used a Velostat strip pressure sensor to characterize the lower limb pressure in adaptive tests in prosthesis. Niu *et al.* [27] evaluated athletic helmet's comfort and stability level based on the data acquired from a flexible pressure sensor array in the helmet. In the above emerging areas as customized and remote healthcare, tele-sportscare, etc., Velostat pressure sensors have been playing an increasingly important role in providing original signals for subject monitoring.

However, compared with rigid piezoresistive sensors made of crystals such as silicon and metals, Velostat pressure sensors commonly suffer certain extent of performance disadvantages such as inferior repeatability, hysteresis and nonlinearity, which originate from some notorious defects of such polymeric material, including certain degree of plastic deformation, non-uniformity in material composite and texture [28]. Moreover, when used in sensor arrays, due to the plastic characteristic of Velostat and the chaotic currents in the resistor array, considerable crosstalk in neighboring grids has been consistently observed [29]. Furthermore, the non-uniformity in material composite and texture have also contributed to even the non-uniformity in the crosstalk. The above common issues with Velostat sensors would be challenging for conventional signal compensation methods. Fortunately, recent advancement in information fusion and processing have opened up a new window in signal processing and enhancement [30]. Particularly, the powerful artificial intelligence, machine learning etc. have found their applications in addressing the otherwise tenacious problems as in the Velostat pressure sensors and arrays.

In the work reported in this paper, a 27×27 Velostat piezoresistive sensor array for object recognition through pressure pattern identification is demonstrated. Three experiment setups are first developed to ensure the accuracy, reliability and consistency of the signal generation, data rendering and interpretation. Through the following experiments with the setups on systematic material characterizations and sensor calibrations, a baseline tactile signal database is established. Using ResNet-PI, a high-precision recognition CNN, the aforementioned system issues associated with material properties of Velostat, have been effectively tackled. The contributions of this paper are:

1. Systematic material study on the polymer composite in Velostat to understand the electrical and mechanical characteristics of the conductive material. The resistivity of the material as a function of applied pressure is studied, and the quasi-static response is also characterized.
2. Tactile sensor array design and establishment of three experiment setups and data processing scheme for quantitative evaluation of the performance of the Velostat sensor array using both electronic signals and imaging processing. The first setup is to establish a baseline for optimized response of the system, in which a series of objects with the same weight but various shapes are used for pattern identification. In the second and third setup, quasi-static responses of the system are characterized, with rise, fall and settling transients being studied, respectively.
3. Based on the data obtained from the three experimental setups, a contrast enhancement algorithm was adopted to counteract the crosstalk effect widely exists in such systems. In the above implementation, ResNet-PI, a residual convolutional neural network was employed for pressure image recognition. With 10 object pressure images to be processed, a precision of 0.9854 was observed.

The presentation of the work is as follows. In Section II, the issues with Velostat sensors in the current related research are briefly introduced. Based on the observations of the challenges to be addressed, the methodology of this research is described in Section III, followed by the presentation of experimental results in Section IV. Some discussions of the results and future work are given in Section V prior to the conclusion drawn in Section VI.

II. Current Challenges for Velostat Sensors

With the increasing demand for smart life systems, Velostat, an emerging functional material with great flexibility, is widely used in the fabrication of piezoresistive sensor arrays. However, the current research of piezoresistive sensor array based on Velostat has the following problems.

The past research on Velostat has been focused on characterizations of the electrical and mechanical properties associated with particular applications of the material. In [28] and [31], piezoresistive sensitivity, hysteresis, repeatability, etc. have been investigated. Some researchers have confirmed the usability of the material in terms of hysteresis and repeatability. In addition, other papers do not have a unified measurement unit (Newtons; Pascals) [32]. Our research found that the use of Pascals is an inappropriate measurement unit for the Velostat sensor. It's well known that various parameters related to the deployment of Velostat material as a sensing element are involved when such a sensing system is constructed. For instance, when used as a force sensor where Velostat material is made contact with certain electrodes as measuring instrument, the changes of the Velostat sensor resistance are a function of the following factors: Velostat material properties, applied force and applied time, the contact area between the measuring instrument and the Velostat sensor, the area of the intersection of the conductive wire, and the relative position of the center of the measuring instrument and the intersection of the conductive wire, etc. However, thus far, not too much research has been conducted on the relations between the resistance of Velostat sensor and the applied

pressure and applied time from the application perspective of object recognition. In our research using the Velostat sensor as the piezoresistor, the relative position of the element and the force measuring instrument is relatively static - the probe of the force measuring instrument is always located in the center of the measured element, which allows us to maintain other conditions unchanged to characterize the pressure response of the sensing element. Based on our systematic studies on the piezoresistive responses of Velostat, including the sensitivity and resistance changes under different pressures and times, we have proposed appropriate experiment setups with specific object weight to obtain higher recognition accuracy.

In design the above particular experiment setups for our purpose, we have addressed some practical issues in previously reported applications of Velostat sensors. Dzedzickis *et al.* [32] reported the effects of surface roughness of new and used Velostat materials, as well as the loading, on the stability of sensor responses. Other researchers [26], [33] have investigated the overall time dependence of the output voltage of the Velostat sensors. However, none of the above research has drawn a conclusion as when data acquisition should be performed after the force or pressure is applied to the sensor for reliable image construction.

This happens to be one of the most critical influencing parameters in establishment of a pressure image database. On one hand, if the collection time is too short, a large amount of pressure image information under different conditions will be lost. On the other hand, if the collection time is too long, redundancy occurs with large number of duplicated data in the dataset, which will reduce the processing resources. We investigated this issue by characterizing the data acquisition system of the Velostat sensor array by examining the transient response of the sensor resistance systematically. Comprehensive studies on steady-state values, variance, rise, fall, and settling transients in unloaded, loaded, and released states of the sensor array resistance are conducted to find the optimal responses of the sensor array. An experiment setup and measurement scheme for optimization of data collection and release time has been established to ensure the diversity, richness and universality of pressure image data sets.

The crosstalk is a critical issue that affects the image recognition accuracy. It originates from both mechanical and electrical responses of the sensor. Mechanical crosstalk is caused by the non-ideal force diffusion of the flexible material under pressure [34]. Due to the length limit of the manuscript, electrical crosstalk will be focused in this study, while mechanical crosstalk being left as one of our future works as mentioned in Section V. Electrical crosstalk is a widespread problem in resistive sensor arrays, which usually causes loss of accuracy [35]–[37] and ghosting [38]. The electrical crosstalk can be divided into two types, i.e., electrical crosstalk Type A and Type B. The Type A crosstalk is caused by the random current flowing through the Velostat resistance in related areas in the sensor or sensor array. Particularly, for the sensor structure used in this paper, this type of crosstalk is related to the surface resistance of the Velostat material. Based on the observation that compared with the bulk cross-sectional resistance that is employed for pressure sensing, the resistivity of the surface layer is relatively low in thickness direction (<31,000 ohms/sq.cm; www.adafruit.com/product/1361), the sensing error caused by this resistance element is relatively small thus can be neglected. Detailed study in the effect of such surface resistance will be reported in future. Electrical crosstalk type B is due to the fact that current always flows through a path with smaller resistance, which is a critical element in determination of performance of the sensor in this study. The proposed experimental setup aims at addressing this crosstalk particularly. The cause of the specific Type B electrical crosstalk is that when calculating the resistance of a target piezoresistive sensor element (cross spot), not only the current flows through this target piezoresistive sensor, but also through the adjacent sensors. It's equivalent to a parallel connection of several piezoresistive sensors. Many researchers have proposed many solutions [39], [40] in this regard. Hidalgo-López *et al.* [29] add additional calibration rows and columns to the original resistance array. Suprapto *et al.* [41] used diodes to shield the reverse current of each sensor. Yet, most of the methods are inadequate in ensuring needed flexibility and signal-to-noise ratio (SNR) of resistor arrays. To address this challenge, we choose a "zero potential method" in which operational amplifiers are used as auxiliary circuits for SNR boost. Consequentially, the contrast of the pressure image can be enhanced to suppress the crosstalk effect.

In addition to the physical sensing element, image processing is also essential for the force and pressure image system demonstrated in this work. Most of previous researchers have used conventional linear scaling (normalized) scheme in generation of pressure images [22], [42], in which the low SNR caused by crosstalk and electrical noise, along with pressure signal spikes, cannot be effectively managed in the algorithm. Using CNN to recognize and classify tactile images has proven to be an effective method [43]–[45]. For real-world tactile perception applications such as identification and analysis of grasping, sitting, gait, etc., classification tasks are dynamic and continuous [52]–[56]. Although it could be extended to series image data sets processing, the purpose of this paper is to develop solutions based on the particular characteristics of the Velostat pressure sensor array we have demonstrated, and some major interferences such as crosstalk. The Velostat sensor array combined with the CNN framework provides a feasible solution and mechanism for future enhancement and applications. Current work reported in this paper mainly focuses on fundamental mechanism of the sensor array - a smart cushion that has been implemented to realize human sitting posture recognition [57]. In our design, CNN based contrast enhancement is used to counteract the influence of crosstalk and electrical noise, and eliminate the signal spikes. According to the size and resolution of the pressure images, ResNet-PI, a modified version based on ResNet18, has been demonstrated in this paper to recognize objects. Totally 12 different contrast enhancements (3 kinds of enhancements, 4 possible coefficients for each enhancement) using ResNet-PI have been implemented with the best accuracy.

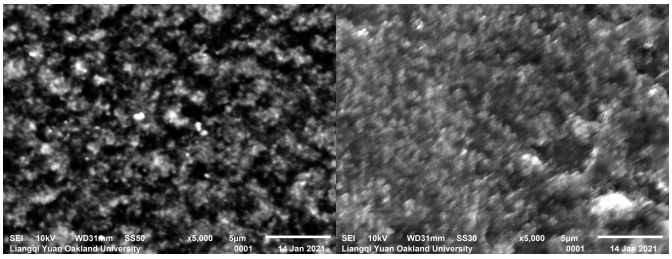

(a) (b)

Fig. 1. SEM image of Velostat material at 5000 times magnification, (a) without pressure and (b) with pressure.

III. Methodologies

A. Velostat Material

Velostat material is flexible, stretchable, light and thin (0.1mm thick), and low in price (11 inches by 11 inches material price is $ 4.95). As a polymer composite material, Velostat consists of carbon-impregnated polyethylene, a resistive material based on quantum tunneling and percolation [32], [46]. Through scanning electron microscope (SEM), the changes of carbon particles (white area) and gap (black area) under pressure can be observed, as shown in Fig. 1 is the surface of Velostat with a magnification of 5000x. When no pressure is applied, the gaps between the polymer clusters measure an average value of 1 micron. Under pressure, the gap is statistically reduced to approximately 0.6 microns. When pressure is applied, the gap becomes smaller, and the effective distance between the conductive elements decreases, thus the overall conductivity of the material increases.

According to the model for conductive polymer composite materials established by Zhang *et al.* [47], the relative resistance of the composite material at any applied time t of pressure can be expressed as:

$$\frac{R(t)}{R_0} = f(\sigma, D, \theta, \varphi, \varepsilon_0, \psi, n) \tag{1}$$

where $R(t)$ is the instantaneous resistance of the composite material at applied time t; R_0 is the original resistance, σ is the applied pressure, D is the nominal diameter of the filler particles, θ is the filler volume fraction, φ is the potential barrier height, ε_0 is the original strain, ψ and n are constants related to creep behaviors in the material. When these factors are fixed, the relative resistance is only related to t, and the relative resistance decreases as t increases [47]. In our experiment, the applied pressure σ which as the object weight also needs to be taken into consideration. We fix other factors unchanged and consider σ and t as independent variables separately. At the same time, the resistance of the polymer composite material R rather than the relative resistance is studied as a dependent variable. Equation (1) can be rewritten as:

$$R(\sigma; t) = f(\sigma; t|D, \theta, \varphi, \varepsilon_0, \psi, n) \tag{2}$$

Velostat is used as the piezoresistive resistor in our sensor array design. Except for pressure, there are similarities such as tension and mechanical bending will also decrease the resistivity of Velostat. Fig. 2 shows a schematic diagram of the changes in the gap (black area) and conductive carbon particles (white dot) inside the Velostat when pressure, tension, and mechanical bending are applied to Velostat.

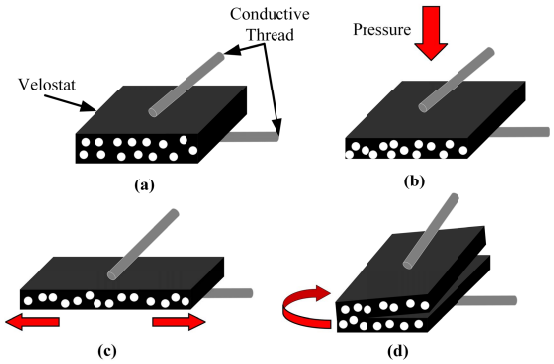

Fig. 2. Velostat cross-sectional schematic diagram, (a) normal state; (b) with pressure; (c) tension applied; and (d) mechanical bending.

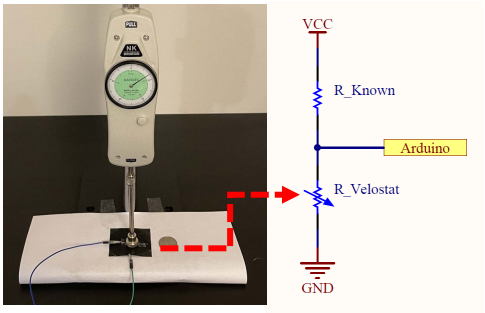

(a) (b)

Fig. 3. Evaluation method of Velostat resistance sensitivity, (a) push pull force gauge and (b) measuring circuit.

B. Test Setup

In order to test the influence of the applied pressure σ and applied time t on the Velostat resistance, a setup with a push-pull force gauge (Max Load 500 N Stand Tester) was designed in this research, as shown in Fig. 3 (a). The setup features a single-input single-output (SISO) characterization scheme, as illustrated in Fig. 3 (b).

The resistance of Velostat was calculated using Arduino Uno and breadboard. Fig. 3 (b) shows the schematic diagram of the circuit. The basic principle is a voltage divider circuit. The resistance value of Velostat can be calculated by:

$$\mathrm{R}_{Velostat} = \mathrm{R}_{Known} \frac{V_{out}}{V_{cc} - V_{out}} \tag{3}$$

where $\mathrm{R}_{Velostat}$ is the resistance value of Velostat, R_{Known} is the known resistance value, V_{out} is the output voltage, which is the voltage converted from the value read by the Arduino analog pin, and V_{cc} is the power supply voltage. Push Pull Force Gauge is used to apply different pressures and different times, and the results are presented in Section IV-A and Section IV-B.

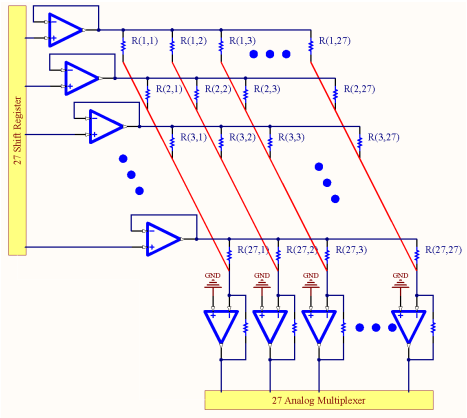

Fig. 4. The schematic circuit diagram of the sensor array uses 27 shift registers (4 chips) and 27 analog multiplexes (4 chips) to select the rows and columns to be read. Each row and column have a grounded operational amplifier to reduce the impact of crosstalk.

C. Sensor Array Fabrication

In order to use the piezoresistive resistance material Velostat to obtain the pressure information of the object. We have fabricated a tactile sensor array with 27 rows and 27 columns. A total of 729 sensors are composed of piezoresistive resistance Velostat. We chose the zero-potential method [39], [48] based on electrical grounding. This method does not require the insertion of diodes or crystals to affect the sensor array's flexibility, and the impact on SNR is minimal. Furthermore, use shift registers and analog multiplexers to scan the entire sensor array row by row to obtain each sensor array point's value. Each element in the sensor array is a pixel on the generated pressure image. Fig. 4 shows the circuit structure of this method.

As noted in Fig. 4, $R(i, j)$ is the sensor element in the ith row and jth column of the piezoresistive resistance sensor array made by Velostat. Velostat sensor array has a seven-layer structure, and it is a symmetrical structure. The top and seventh layers are protective layers. It is covered with a 0.0127 mm PVC protective film. This protective film is transparent, soft, thin, and cheap. It not only maintains the robustness of the sensor array, but also does not weaken the pressure signal of the object. The second and sixth layers are adhesion layers, using 0.236mm adhesive transfer tape acrylic to ensure the firmness of the protective layer and the relative position of the conductive thread and Velostat. The third and fifth layers are the column conductive and row conductive layers, using conductive threads made of stainless-steel fibers, which are soft, easy to fabricate, and have low resistivity. The fourth layer is Velostat material. The structure diagram of the sensor array is shown in Fig. 5.

The remaining signal processing circuit consists of operational amplifiers, shift registers, analog multiplexers, and Arduino Nano. Arduino Nano scans each element's value by switching rows and columns, and after digital signal processing, it sends each element's value to Processing to generate a picture. Fig. 6 shows the PCB and sensor array of the signal processing circuit. To facilitate the second production in the later stage, the DuPont line is used as the connecting line.

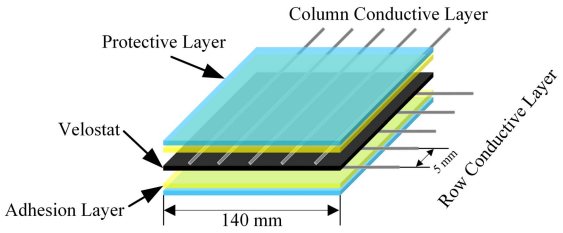

Fig. 5. The schematic diagram of the sensor array, where blue is the protective layer, yellow is the adhesion layer, the silver thread is the conductive thread, and the black is Velostat.

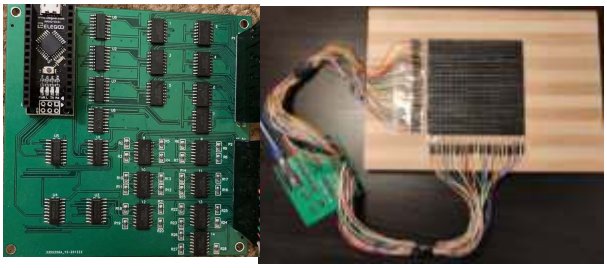

(a) (b)

Fig. 6. Sensor array hardware system, (a) the top view of the PCB and (b) the overall hardware circuit used to collect object pressure information includes the PCB and the sensor array.

D. Quasi-Static Response

Each element of the Velostat sensor array corresponds to each pixel on the pressure image. Due to the non-necessity and inaccuracy of the secondary resistance calculation, here we directly use the reading of the Arduino Nano as the value of the pixel, which is called the conductance G. For applied pressure σ and applied time t that affect the Velostat sensor array resistance in (2), it is more appropriate to study the relationship between σ and resistance, and the relationship between t and conductance. Since the Velostat sensor array resistance has a higher dynamic range than the conductance, the curve of σ and resistance can more realistically reflect the changing trend. Applied time t as a key factor of generating pressure images, directly affects the diversity and quantity of pressure image data sets, so the curve of t and conductance is more suitable for discussion.

Quasi-static response is defined to express the relationship between t and conductance G. According to our experience, during the process of applying pressure to the Velostat, the increase rate in the element conductance will slow down. After a long enough time, the element conductance will reach a steady state. First, we define the steady-state conductance values in three states:

$$\overline{G_{state}} = \frac{1}{\tau}\left(\sum_{i=T_{state}-\tau+1}^{T_{state}} G_{state}(i)\right) \quad \text{for } state \in \{unl, load, rel\} \tag{4}$$

where $state$ represents three possible states. G_{unl} represents the conductance in the unloaded state, G_{load} represents the conductance in the loading state and G_{rel} represents the conductance in the release state. T_{state} represents the total time

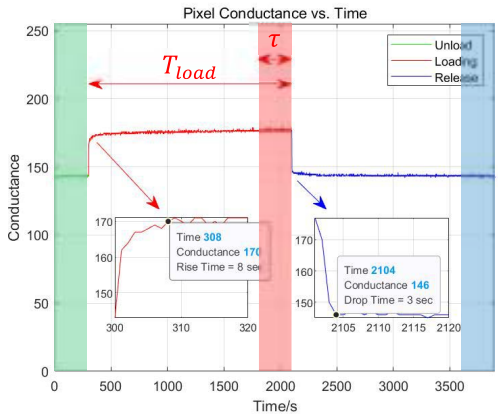

Fig. 7. Conductivity change curve of continuous collection of unloaded $T_{unl} = 5$ minutes, then loaded for $T_{load} = 30$ minutes and then released for $T_{rel} = 30$ minutes. The green, red and blue curves represent the conductance values in the unloaded, loaded and released states, respectively. The green, red and blue shaded parts represent the steady state of unloaded, loaded and released states for a unit time length τ.

of a single *state* continuously collected, for each state we use same formula, but T_{state} is different for each state. $G_{state}(i)$ represents the i-th conductance value in the continuously collected element conductance. Due to electrical noise and disturbance, the conductance is in an oscillating state. The steady-state value is obtained by averaging the last unit time length τ in the duration of each state. The green, red and blue shaded parts of Fig. 7 show the steady state of unloaded, loaded and released states.

Whether the element undergoes plastic deformation before and after loading is also concerned. The difference $diff$ between the unloaded state and the released state is defined as:

$$diff\,(\%) = \frac{\left|\overline{G_{unl}} - \overline{G_{rel}}\right|}{\overline{G_{unl}}} \times 100\% \tag{5}$$

We are interested in how long it takes for an element's conductance to reach an acceptable value. Three quasi-static responses are defined to show the performance of the sensor array conductance. Without loss of generality, the acceptable conductance value is a percentage of the steady-state value, noted by μ. In our experiment, $\mu = 80\%$ (or 90%) is used as the percentage. Rise transient t_r of the element conductance from the start of loading until it rises to the acceptable conductance value is defined as:

$$t_r = \underset{i \in T_{load}}{argmin}\, G_{load}\,(i) \geq \mu_{load}\left(\overline{G_{load}} - \overline{G_{unl}}\right) + \overline{G_{unl}} \tag{6}$$

Similarly, fall transient t_f of the element conductance from the start of release until it falls to the acceptable conductance value is defined as:

$$t_f = \underset{i \in T_{rel}}{argmin}\, G_{rel}(i) \leq \overline{G_{load}} - \mu_{rel}\left(\overline{G_{load}} - \overline{G_{rel}}\right) \tag{7}$$

t_r and t_f as the quasi-static response we are most concerned about are shown in Fig. 7. Stability is the relative difference between the conductance value and the steady-state value is less than a percentage, noted by δ. In our experiment, $\delta = 10\%$ is used as threshold. Settling transient t_s is defined as the element conductance from the start of the state to reach and stabilize at δ of $\overline{G_{load}}$ or $\overline{G_{rel}}$:

$$t_s = \underset{i \in T_{state}}{argmin}\, \frac{\left(G_{state}\,(i) - \overline{G_{state}}\right)}{\overline{G_{state}}} \leq \delta_{state} \quad for\ all\ t_s \leq i \leq T_{state} \tag{8}$$

The results of quasi-static response are presented in Section IV-B.

E. Contrast Enhancement

Since the piezoresistive material Velostat can be regarded as a resistance in both the unloaded and loaded state, the conductance of the sensor array is non-zero even in the unloaded state. And due to the fabrication differences of the sensor array, electrical noise, and different element positions, the initial conductance of each pixel is different. In order to initialize the bias on each pixel and prevent the conductance from becoming negative, the conductance of each pixel has been continuously collected for a period of time in advance to calculate the mean and standard deviation. Each pixel's original conductance subtracts mean to initialize the bias and then adds 4 standard deviations to prevent it from becoming negative.

$$\boldsymbol{G}'(i) = \boldsymbol{G}(i) - \boldsymbol{Mean} + 4\boldsymbol{Std} \tag{9}$$

where $\boldsymbol{G}(i)$ is the original conductance matrix of the sensor array at the i-th moment. $\boldsymbol{G}'(i)$ is the initial conductance matrix after the bias is eliminated at the i-th moment. $\boldsymbol{Mean}$ and $\boldsymbol{Std}$ are respectively the mean and standard deviation of the conductance matrix collected for a period of time (1 hour) in advance.

After obtaining the initialized conductance matrix through (9), the next step is to enhance the contrast between the signal and noise in the pressure image. We assume that the output span of pixel conductance is divided into low output span and high output span. As the pressure increases, the pixel conductance increases and moves from low output span to high output span. At the same time, the distribution of electrical noise remains unchanged. What we can expect is that there is a high amount of electrical noise and a low amount of signal in the low output span. Conversely, there are high amount signal and low amount noise in the high output span. The essence of the designed contrast enhancement is to increase the high output span while maintaining or weakening the low output span. We have selected three candidate functions. One Boolean function is the thresholding and two nonlinear scaling functions are power and exponential. Thresholding is our priority as the simplest way to increase the contrast. The formula for thresholding can be expressed as:

$$\boldsymbol{G}''_{\text{thld}}(i) = \begin{cases} 255, & \boldsymbol{G}'(i) \geq \gamma \\ 0, & \boldsymbol{G}'(i) < \gamma \end{cases} \tag{10}$$

where $\boldsymbol{G}''_{\text{thld}}(i)$ is the threshold contrast enhanced conductance matrix of the sensor array at the i-th moment. γ is a custom

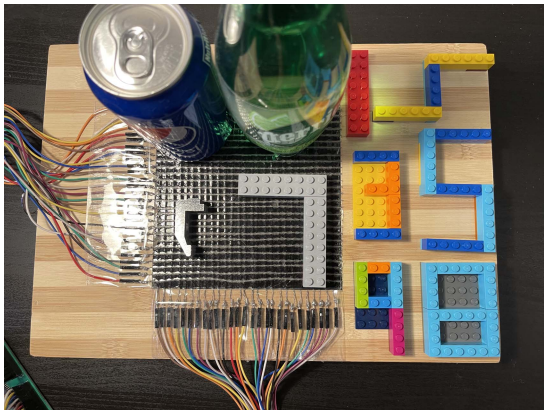

Fig. 8. Ten objects used to collect object pressure information, the order from left to right and top to bottom is Pepsi; Perrier; one; two; iron block; seven; three; five; nine; eight. Since four, six and nine are easily confused, only one of them is selected. Pepsi, Perrier and iron block collect the bottom pressure image in the direction shown in the figure. Seven LEGO numbers are flipped to collect pressure images of the numbers side.

threshold coefficient to be tested for the best result. Thresholding needs to traverse each pixel in $\boldsymbol{G}'$, if the pixel value is greater than γ, it is signal, and if it is less than γ, it is noise. Power and exponential are used as common nonlinear scaling functions, and they directly calculate $\boldsymbol{G}'$. The formula of power can be expressed as:

$$\boldsymbol{G}''_{\text{power}}(i) = \boldsymbol{G}'^{\alpha}(i) \tag{11}$$

where α is a custom power coefficient to be tested for the best result. The formula of exponential can be expressed as:

$$\boldsymbol{G}'_{\text{exp}}(i) = e^{\beta \boldsymbol{G}'(i)} \tag{12}$$

where β is a custom exponential coefficient to be tested for the best result. The results from these 3 kinds of contrast enhancements are presented in Section IV-C and Section IV-D.

F. Convolutional Neural Network

Convolution neural network (CNN) has been widely used in computer vision for object recognition. In our experiment, we also apply CNN to pressure images for the CNN can extract feature vectors in the pressure image to calculate the probability of an image's category for matching. We have selected 10 objects for testing, with 7 objects are distinguishable shape numbers made by LEGOs, and 3 objects from daily life, including an iron block, a Pepsi can and a Perrier bottle, as shown in Fig. 8. These objects were chosen because of their rigidity, distinguishable contours, and low surface area characteristics. Combining three experimental setups, the pressure image data set was collected by placing these objects at different positions in the Velostat sensor array at different rotation angles.

In order to use CNN to classify these objects, a residual neural network based on ResNet18 [49] was developed. Fig. 9 shows the block diagram of the modified version of ResNet for Pressure Image (ResNet-PI) in this work. To make the neural network more suitable to the collected pressure images

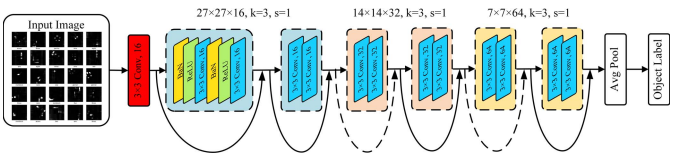

Fig. 9. The ResNet-PI block diagram used in this paper. ResNet-PI has 3 ResNet layers, and each ResNet layer has two basic blocks (dashed blocks). The ResNet layer is distinguished by different fill colors (blue, red, yellow), and down-sampling (dashed line) is required between the two ResNet layers. In order to save space, only the first basic block is drawn completely. Each basic block is composed of convolution filter (Conv), batch normalization (BaN) and rectified linear unit (ReLU). The two layers are connected by skip layer. Finally, the output of the ResNet layer performs the average pooling (Avg Pool) operation and uses Dense to output the label of the object.

(with a low resolution of $27 \times 27 \times 1$) in this work, a simplified ResNet-PI scheme modified from ResNet-18 is adopted to reduce the number of convolutional layers and CNN parameters for a more lightweight CNN architecture. It is implemented in TensorFlow. To detail the configuration, the size of the initial convolutional layer is set as 3×3, the stride as 1, the number of initial filters as 16, and the total number of layers as 14. With such a lightweight CNN and low-resolution image data set framework, this configuration not only guarantees overall performance sufficient to our requirements, but also provides a potential real-time solution for other dynamic tactile applications. The initial learning rate is 10^{-3}, the learning rate becomes 0.1 times the initial learning rate after every 100 epochs of training. A total of 200 epochs are trained. The batch size is 32, and the selected loss function is classification cross-entropy.

IV. Experiments and Results

To obtain a high-quality pressure image data set, we conducted experiments on two important parameters object pressure σ and applied time t that affect the resistance of Velostat. For σ, the resistance sensitivity of the SISO sensor and a single element in the sensor array were measured respectively, and the ideal object weight was found. For t, the sensor array quasi-static response was measured, and the appropriate collection time and release time were found. These three experiment setups were used to build the original pressure image data set. Three kinds of contrast enhancements are used to process the original pressure image data set, combined with ResNet-PI to find the best accuracy Contrast Enhancement and recognize 10 objects.

A. Resistance Sensitivity

For the research of resistance sensitivity, the influence of applied time t should be eliminated as much as possible. The recording time is fixed to be one-second delay after the pressure is applied. To reduce the jitter and the inaccuracy of delay recording, the experiment was repeated three times and the measurements were averaged. Moreover, there was an interval of 1 hour between each experiment to restore Velostat to its initial state.

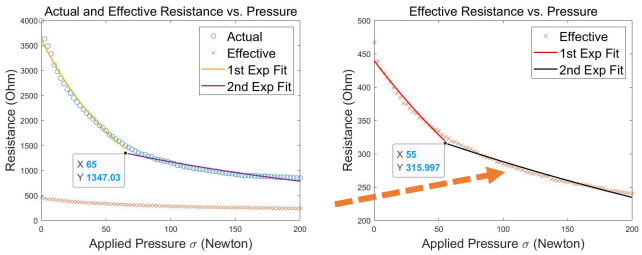

Fig. 10. Resistance vs. pressure curve, (a) actual resistance and effective resistance comparison, the two exponential curves fitting of the actual resistance, and the actual resistance intersection point is 65 Newtons; (b) Effective resistance with pressure curve, the two exponential curves fitting of the effective resistance, the effective resistance intersection point is 55 Newtons.

Since the resistance sensitivity of the sensor array is a direct factor in generating the pressure image, a single element in the sensor array is more worthy of attention. The resistance of a single element on the sensor array will be affected by crosstalk, and its resistance will be greatly reduced. We define the resistance of a single element in the sensor array as the effective resistance, and the resistance of the SISO sensor that is not affected by crosstalk as the actual resistance. The actual resistance and the effective resistance are compared to observe the effect of crosstalk on the sensor array. Using the circuit shown in Fig. 3 and (3), pressure is applied to Velostat sensor cyclically, to obtain the relation of the actual resistance and the effective resistance versus applied pressure σ.

Fig. 10(a) shows that as σ increases, the actual resistance decreases exponentially in two exponential curves, the first curve will be faster and the second curve will be slower. The actual resistance intersection of these two exponential curves is 65 Newtons, which means that the actual resistance of Velostat sensor is more sensitive to pressures less than 65 Newtons. At the same time, under the same pressure, the effective resistance is almost equal to one tenth of the actual resistance. The huge reduction in the sensor array sensitivity caused by crosstalk will be eliminated by contrast enhancement, and the result are presented in Section IV-C and Section IV-D.

Fig. 10(b) shows the same properties of effective resistance. When σ increases, the effective resistance decreases exponentially in two exponential curves, the intersection is 55 Newtons. According to these 2 intersections, the ideal weight of the object is around 60 Newtons. If the object is too light to be recognizable, additional weight (up to 60 Newtons) needs to be applied to make sensor array resistance fall to a recognizable value. This is leads to the first experiment setup.

Experiment Setup 1 (Object Weight): The ideal object weight is around 60 Newtons for high accuracy.

It is worth noting that although in our experiments, the characteristic of the faster exponential curve is not used as one of the experimental setups, it is a versatile characteristic that deserves attention. Although the selected 10 rigid and easily distinguishable objects will bring higher accuracy, the pressure of the objects is evenly distributed on several elements due to their uniform texture. If due to uneven texture or objective pressure distribution, this may bring more achievable functions to the Velostat sensor array, which will be one of the future works.

TABLE I
PARAMETER SETTING OF SENSOR ARRAY PERFORMANCE MEASUREMENT

τ (mins)	T_{unl} (mins)	T_{load} (mins)	T_{rel} (mins)	μ_{load}	μ_{rel}	δ_{state}
5	5	30	30	80%	90%	10%

B. Quasi-Static Response

According to experiment setup: object weight, when the selected object weight is determined and the object shape is independent, we turn our attention to the applied time t, which is the quasi-static response of the Velostat sensor element.

To obtain the steady-state element conductance in the three states of unloaded, loaded, and released, unit time τ needs to be set. The difference between the mean for 5 minutes and 60 minutes of the unloaded state is less than 0.1%. So $\tau = 5$(mins) is considered to be an appropriate value, short enough not to waste time and enough to reflect the steady state. The unloaded state only records a unit time length $T_{unl} = \tau = 5$(mins). Taking into account the situation of long-term use, the loaded and released states collect the total time length is $T_{load} = T_{rel} = 30$(mins) to observe their changes. In the long-term pressure application, there will always be a period of slow rise in conductance, which is unnecessary for collecting pressure image data sets. Therefore, compared to the released state, set $\mu_{load} = 80\%$ to eliminate the interference of the slow rise of the loaded state. Due to the low resolution of Arduino Nano (8-bit ADC), the conductance will oscillate even in steady state. This kind of oscillation is acceptable, and what we care about is whether there is a general tendency for the conductance. $\delta_{state} = 10\%$ is set to eliminate the influence of oscillation, and the main measurement is when the general trend of change ends. The settings of these parameters are shown in TABLE I.

Using the setup shown in TABLE I, four pixels of index (5,1), (10, 1), (15,1) and (20,1) were tested under a force of 100 Newtons. 65-minute pixel conductance change curve shown in Fig. 11 and the performance measurement results shown in TABLE II were obtained.

To ensure the diversification of the data set, a lower sampling rate and appropriate sampling time are essential. The lower sampling rate is set to 1 sample/sec in our experiment. Appropriate sampling rate needs to ensure the number and difference of pressure images in the data set, which can be determined by t_r. Fig. 11 and TABLE II show that in the first $t_r = 10$ seconds, the conductance quickly rises to an acceptable value. t_{s-load} of each element is greater than 1000 seconds, which proves that the conductance rises slowly under long-term pressure, and this rise is small enough to be ignored. In order to avoid repeated pressure images and the

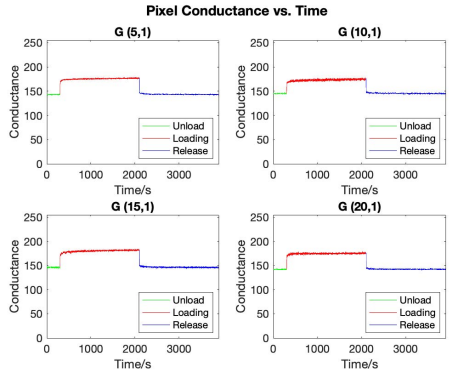

Fig. 11. Conductance change curve of four pixels in three states. The green, red and blue curves are unloaded, loaded and released states respectively.

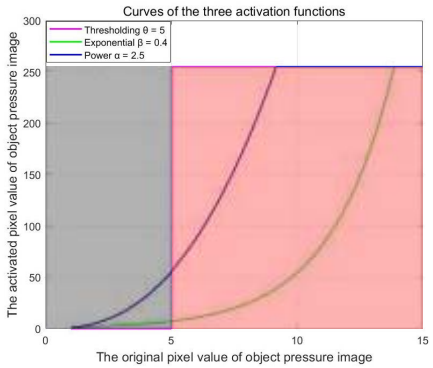

Fig. 12. The curves of the three activation functions and the areas of noise and pressure information. The curves of the three contrast enhancements and the areas of noise and pressure information. The black shadow is noise and the red shadow is the signal.

TABLE II
PERFORMANCE OF 4 PIXELS CONDUCTANCE UNDER UNLOADING, LOADING AND RELEASING STATES

	$G(5,1)$	$G(10,1)$	$G(15,1)$	$G(20,1)$
G_{unl}	143.1967	145.1033	146.5367	141.9467
		Loading		
$\overline{G_{load}}$	176.6200	174.5400	181.8167	175.5233
G_{p-load}	179	178	184	179
$t_r(s)$	8	10	13	8
$t_{s-load}(s)$	1285	1789	1105	1773
		Release		
$\overline{G_{rel}}$	143.8339	145.5847	146.7375	142.2259
G_{p-rel}	142	143	143	140
$t_f(s)$	3	2	4	2
$t_{s-rel}(s)$	89	28	96	38
$diff(\%)$	0.44	0.33	0.14	0.20

element rises to an acceptable value, the collection time is defined as 10 seconds to ensure the diversity and universality of the pressure image data set. Based on these facts, the second experiment setup is proposed as the following.

Experiment Setup 2 (Collection Time): Only the first 10 seconds of pressure images should be continuously recorded.

In order to ensure that the pressure images are collected with the same initial conditions each time, it is essential to release after the sensor array is used. The release time is usually specified by t_d and t_{s-rel} in Fig. 11 and TABLE II, t_f is less than 5 seconds, and t_{s-rel} is less than 100 seconds. In order to reduce unnecessary waste of time, the pressure images are collected for 10 seconds (experiment setup: collection time) and then perform a short release. Such a collection action lasted 30 minutes and then perform a long release. This short release is given by t_d, and the long release is given by t_{s-rel}. We slightly extend both release transient t_d and t_{s-rel} to ensure that each element on the sensor array is released enough. The short release time is defined as 5 seconds, and the long release time is defined as 100 seconds. The difference between unloaded and released is given by $diff$. It can be seen that the difference of each element is less than 1%, which shows the excellent repeatability of the sensor array. So, the third experiment setup is stated below.

TABLE III
VELOSTAT SENSOR ARRAY CHARACTERISTIC PARAMETERS

Preset Pressure	Resolution	t_r	t_f	t_{s-load}	t_{s-rel}
60 N	1 Pixel/5 mm	≈10 s	≈5 s	$>$ 1000 s	$<$ 100 s

Experiment Setup 3 (Release Time): After continuous collection of images each time, 5 seconds are required to release. After 30 minutes of collection, an additional 100 seconds must be released.

The entire system, including the sensor array and signal processing subsystem, only costs approximately 45 US dollars and demonstrates considerable characteristic parameters, as shown in TABLE III.

Comprehensive characterization of the Velostat sensor array has been conducted prior to signal processing of the acquired pressure images in the three experiment setups. The following Sections IV-C and IV-D detail the method and procedure foraccuracy improvement through contrast enhancement and appropriate ResNet-PI classification.

C. Contrast Enhancement

In order to apply contrast enhancement to pressure images, we first need to initialize the pixel conductance. The readings for 1 hour are collected to calculate ***Mean*** and ***Std*** in (9), only 9 pixels conductance are shown here for discussion. TABLE IV shows the detailed information of these 9 pixels conductance.

Although the low variance and standard deviation (less than 1) show that the sensor array is very stable in the unloaded state. But due to sensor fabrication and electrical noise, each pixel conductance mean on the sensor array is unevenly distributed in the interval 136 to 149. This uneven distribution and high bias will affect the sensitivity and recognition accuracy of the pressure image. Equation (9) is used here to subtract bias and initialize the sensor array. After getting the initialized pressure image, Equation (10) is used to enhance the contrast of the pressure image. According to original pressure image data set, the initialized pressure image conductance changes

TABLE IV
AVERAGE, VARIANCE AND STANDARD DEVIATION OF 9 PIXELS CONDUCTANCE

Pixel Coordinates	Mean	Variance	Standard Deviation
G (1,1)	143.1069	0.5979	0.7732
G (1,10)	141.9957	0.4233	0.6506
G (1,20)	146.1117	0.3794	0.6160
G (10,1)	145.7284	0.4498	0.6707
G (10,10)	142.1016	0.1207	0.3475
G (10,20)	143.9753	0.2105	0.4588
G (20,1)	146.7424	0.4633	0.6806
G (20,10)	142.7388	0.3435	0.5861
G (20,20)	145.2029	0.4600	0.6782

TABLE V
EVALUATION FOR DIFFERENT CONTRAST ENHANCEMENTS AND COEFFICIENTS

Contrast Enhancements	Coefficient	Original Accuracy	Verification Accuracy	Confidence
Thresholding	$\gamma = 2$	0.7800	0.75	96.15%
	$\gamma = 3$	0.8785	0.85	96.76%
	$\gamma = 4$	0.9181	0.80	87.14%
	$\gamma = 5$	0.9220	0.75	81.34%
Power	$\alpha = 1.5$	0.9134	0.90	98.53%
	$\alpha = 2$	0.9751	0.95	97.43%
	$\alpha = 2.5$	0.9813	1.00	98.09%
	$\alpha = 3$	0.9296	0.80	86.06%
Exponential	$\beta = 0.3$	0.9841	1.00	98.38%
	$\beta = 0.4$	0.9854	1.00	98.52%
	$\beta = 0.5$	0.9844	1.00	98.42%
	$\beta = 0.6$	0.9799	1.00	97.95%

from 0-5 (low output span) when it is unloaded, and it changes from 5-15 (high output span) when it is loaded. In order to compare the detection threshold, power and exponential, these three alternative contrast enhancements. CNN is trained for every possible coefficient of each enhancement to compare their accuracy, as shown in TABLE V.

D. ResNet-PI Training and Classification Results

We collected 8066 frames of original pressure images of 10 objects. Following experiment setup: object weight, these 10 objects have been added with additional pressure to reach 60 Newtons. When collecting pressure images, follow the collection time in experiment setup: collection time and the release time in experiment setup: release time. Besides, the original data set was expanded four times by rotation and translation. The whole data set has 32264 frames of pressure images, which is divided into the training data set (22584 frames) and test data set (9680 frames) at a ratio of 7:3.

To investigate the effectiveness of the 3 contrast enhancement methods discussed in Section IV-C, ResNet-PI is used to train pressure images processed by these three contrast enhancements. To verify the universality, repeatability and reliability of the test results, as well as a discussion about the impact of the surface roughness of new and used materials on accuracy, we have set two evaluation criteria. The first evaluation criterion is the Original Accuracy, which is obtained

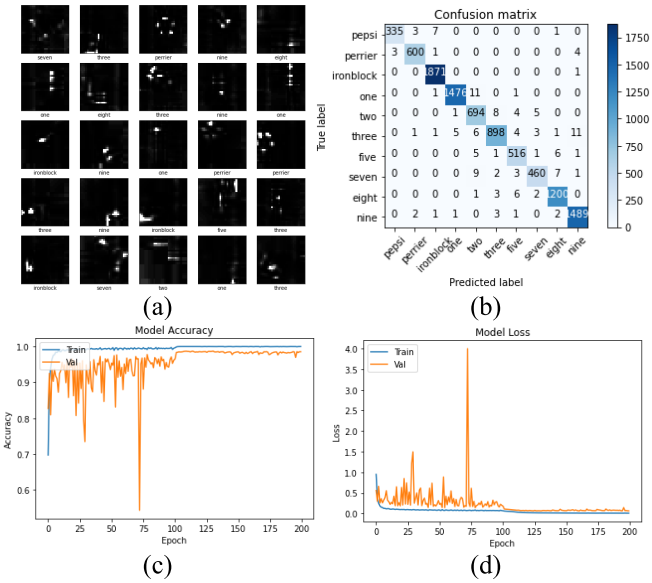

Fig. 13. The training model ResNet-PI, under Exponential and $\beta = 0.4$, (a) 25 randomly selected pressure images that have been enhanced; (b) confusion matrix; (c) model accuracy curve; (d) model loss curve.

by predicting 9680 frames of test data set by TensorFlow. The second evaluation criterion is Verification Accuracy. On the second day, we re-collected the pressure images of 10 objects, 2 frames for each object, 20 frames in total, which were used by TensorFlow predicting the re-collected 20-frame validation data set. We use the similarity between the Original Accuracy and the Verification Accuracy to evaluate whether the Original Accuracy is credible, and name it as Confidence

TABLE V shows that after three alternative contrast enhancements are performed on the original pressure image data set, the accuracy and confidence of ResNet-PI classification. We have selected some representative coefficients to show changes in accuracy and confidence. Thresholding enhancement coefficient γ increases, the low output span becomes larger and the high output span becomes smaller. Thresholding enhancement is too strong to completely reject low output spans and lose some signal information. Power enhancement characteristics are the same as the Exponential, but the Power enhancement is too much affected by α and cannot be easily determined. Also, Power enhancement will not only enhance weak signals to a limited extent, but also not as steep as the Exponential enhancement when strong signals. Exponential enhancement is the best contrast enhancement, with the best accuracy and confidence to be used in this design. Under Exponential enhancement and $\beta = 0.4$, the accuracy of the model reached 0.9854. Fig. 12 shows the curves of the three contrast enhancements at the best accuracy. It can be seen that different enhancements have different abilities to shield noise and activate pressure information.

A few pressure images obtained by Exponential enhancement with $\beta = 0.4$ are shown in Fig. 13 (a). It can be seen that the objects pressure characteristics are clearly visible even in the case of low resolution and noise. The confusion matrix is

TABLE VI
COMPARISON OF ACCURACY BETWEEN RESNET-PI AND 4 OTHER CLASSIFICATION ALGORITHMS

ResNet-PI	AlexNet [49]	VGG19 [50]	ResNet-50 [51]
0.9854	0.9751	0.9659	0.9898

shown in Fig. 13 (b), which can be seen that most of the errors come from similar object pressure images. The main reason may be that the resolution of the fabricated sensor array is not high (the distance between the two pixels is 5mm), and the edge features of object may be in the blank area between two elements. Fig. 13 (c) and Fig. 13 (d) show the accuracy curve and loss curve of the model, respectively. The obvious convergence and close match of the processed data to the training model validate that our model parameter settings are appropriate for such application.

To highlight the advantages of the ResNet-PI we designed, TABLE VI compares several common image classification algorithms. It can be seen that the pressure image data set generated by our Velostat sensor array has distinguishability, which can work on multiple popular CNNs and achieve valuable accuracy. Also, it can be observed that with a much simplified and lightweighted scheme configured to our Velostat sensor array, ResNet-PI demonstrates a remarkable accuracy that's comparable to some other popular CNNs. The performance suggests its great potential in many other dynamic tactile applications where real-time classifications are highly desired.

V. DISCUSSIONS AND FUTURE WORK

A. Crosstalk

Electrical crosstalk can be resolved by contrast enhancement, which has been discussed in this paper. However, mechanical crosstalk is also one of the important causes of low contrast pressure images. Mechanical crosstalk is the mechanical deformation caused by the pressure of the object placed on the Velostat is transmitted to the adjacent elements and the resistance of the surrounding elements decreases at the same time. This mechanical deformation and force transmission effect is caused by the undesirable mechanical properties of the Velostat material. The sensor array can be separated into independent elements to suppress electrical crosstalk and avoid mechanical crosstalk, but this method increases the difficulty of production and may weaken the entire system's robustness. which is one of the future works.

B. Adaptive Coefficient β

Although in this paper we tried several contrast enhancements to find the function and coefficient with the best accuracy, but under the influence of factors such as different fabrics sensor arrays, objects with different shapes, different quality pressure image data sets, etc., the optimal value of coefficient β may be different for each sensor array. One of our future work is to develop a method of adaptive adjustment of the coefficient β, considering that the factors related to the coefficient β are output span, average value, variance, peak value and other mathematical quantities related to the distribution of red and black shadows in Fig. 12.

VI. CONCLUSION

In this paper, an object recognition system based on Velostat sensor array is designed to collect and process object pressure image data sets. The system includes a Velostat piezoresistive sensor array, a signal processing subsystem and an image processing method for contrast enhancement. The parameters, such as pressure σ and applied time t that affect the Velostat material and sensor array output are discussed. According to the resistance sensitivity and quasi-static response, three experiment setups are developed, including object weight, collection time and release time, which can increase the universality, repeatability and reliability. ResNet-PI was developed to recognize and classify 10 object pressure images, and 3 contrast enhancement methods were investigated to process the pressure image data set. ResNet-PI achieves the best recognition accuracy of 0.9854 with exponential enhancement and has excellent properties. In summary, through thorough characterization of Velostat material and sensor arrays, we have demonstrated that such sensor array can be used for generation of reliable pressure images. When combined with an appropriate CNN, the system can be used for human activity recognition and monitoring with considerable accuracy. It can be anticipated that with added recurrent neural networks for time correlation processing, the system presented in this paper can be readily extended to more dynamic tactile applications where real-time pattern recognitions are vital.

REFERENCES

[1] C. Huang, Q. Wang, M. Zhao, C. Chen, S. Pan, and M. Yuan, "Tactile perception technologies and their applications in minimally invasive surgery: A review," *Frontiers Physiol.*, vol. 11, p. 1601, Dec. 2020.
[2] X. Pu, S. An, Q. Tang, H. Guo, and C. Hu, "Wearable triboelectric sensors for biomedical monitoring and human-machine interface," *iScience*, vol. 24, no. 1, Jan. 2021, Art. no. 102027.
[3] X. Chen, Y. Mao, X. Ma, and L. Qi, "A tactile method for rice plant recognition based on machine learning," *Sensors*, vol. 20, no. 18, p. 5135, Sep. 2020.
[4] A. dos Santos, E. Fortunato, R. Martins, H. Águas, and R. Igreja, "Transduction mechanisms, micro-structuring techniques, and applications of electronic skin pressure sensors: A review of recent advances," *Sensors*, vol. 20, no. 16, p. 4407, Aug. 2020.
[5] Y. Wang, Y. Lu, D. Mei, and L. Zhu, "Liquid metal-based wearable tactile sensor for both temperature and contact force sensing," *IEEE Sensors J.*, vol. 21, no. 2, pp. 1694–1703, Jan. 2021.
[6] W. Luo, V. Sharma, and D. J. Young, "A paper-based flexible tactile sensor array for low-cost wearable human health monitoring," *J. Microelectromech. Syst.*, vol. 29, no. 5, pp. 825–831, Oct. 2020.
[7] J. Liang, J. Wu, H. Huang, W. Xu, B. Li, and F. Xi, "Soft sensitive skin for safety control of a nursing robot using proximity and tactile sensors," *IEEE Sensors J.*, vol. 20, no. 7, pp. 3822–3830, Apr. 2020.
[8] L. Zhu, Y. Wang, D. Mei, and C. Jiang, "Development of fully flexible tactile pressure sensor with bilayer interlaced bumps for robotic grasping applications," *Micromachines*, vol. 11, no. 8, p. 770, Aug. 2020.
[9] M. I. Tiwana, S. J. Redmond, and N. H. Lovell, "A review of tactile sensing technologies with applications in biomedical engineering," *Sens. Actuators A, Phys.*, vol. 179, pp. 17–31, Jun. 2012.
[10] F. Wen *et al.*, "Machine learning glove using self-powered conductive superhydrophobic triboelectric textile for gesture recognition in VR/AR applications," *Adv. Sci.*, vol. 7, no. 14, Jul. 2020, Art. no. 2000261.

[11] J. Jang, Y. S. Jun, H. Seo, M. Kim, and J.-U. Park, "Motion detection using tactile sensors based on pressure-sensitive transistor arrays," *Sensors*, vol. 20, no. 13, p. 3624, Jun. 2020.

[12] C. Cheng, S. Xuguang, X. Ning, L. Tong, and L. Chang, "Recent progress in technologies for tactile sensors," *Sensors*, vol. 18, no. 4, p. 948, 2018.

[13] X. Luo and Y. B. Gianchandani, "A 100 μm diameter capacitive pressure sensor with 50 MPa dynamic range," *J. Micromech. Microeng.*, vol. 26, no. 4, Mar. 2016, Art. no. 045009.

[14] Q. Tan *et al.*, "A high temperature capacitive pressure sensor based on alumina ceramic for *in situ* measurement at 600 °C," *Sensors*, vol. 14, no. 2, pp. 2417–2430, Jan. 2014.

[15] N. Marsi, B. Y. Majlis, A. A. Hamzah, and F. Mohd-Yasin, "A MEMS packaged capacitive pressure sensor employing 3C-SiC with operating temperature of 500 °C," *Microsyst. Technol.*, vol. 21, no. 1, pp. 9–20, Jan. 2015.

[16] J. Konstantinova, A. Stilli, and K. Althoefer, "Fingertip fiber optical tactile array with two-level spring structure," *Sensors*, vol. 17, no. 10, p. 2337, Oct. 2017.

[17] K. Shimonomura, "Tactile image sensors employing camera: A review," *Sensors*, vol. 19, no. 18, p. 3933, Sep. 2019.

[18] L. Pan *et al.*, "An ultra-sensitive resistive pressure sensor based on hollow-sphere microstructure induced elasticity in conducting polymer film," *Nature Commun.*, vol. 5, no. 1, pp. 1–8, Jan. 2014.

[19] X. Sun, C. Wang, C. Chi, N. Xue, and C. Liu, "A highly-sensitive flexible tactile sensor array utilizing piezoresistive carbon nanotube–polydimethylsiloxane composite," *J. Micromech. Microeng.*, vol. 28, no. 10, Jul. 2018, Art. no. 105011.

[20] M. Gala, J. Barabas, and M. Kopaskova, "User presence monitoring based on velostat pressure sensors and Arduino platform," in *Proc. IEEE 21st Int. Conf. Comput. Problems Electr. Eng. (CPEE)*, Sep. 2020, pp. 1–3.

[21] A. Fatema, S. Poondla, R. B. Mishra, and A. M. Hussain, "A low-cost pressure sensor matrix for activity monitoring in stroke patients using artificial intelligence," *IEEE Sensors J.*, vol. 21, no. 7, pp. 9546–9552, Apr. 2021.

[22] S. Sundaram, P. Kellnhofer, Y. Li, J.-Y. Zhu, A. Torralba, and W. Matusik, "Learning the signatures of the human grasp using a scalable tactile glove," *Nature*, vol. 569, no. 7758, pp. 698–702, 2019.

[23] D. Chen, Y. Cai, and M.-C. Huang, "Customizable pressure sensor array: Design and evaluation," *IEEE Sensors J.*, vol. 18, no. 15, pp. 6337–6344, Aug. 2018.

[24] D. Chen *et al.*, "Smart insole-based indoor localization system for Internet of Things applications," *IEEE Internet Things J.*, vol. 6, no. 4, pp. 7253–7265, Aug. 2019.

[25] R. Hudec, S. Matúška, P. Kamencay, and M. Benco, "A smart IoT system for detecting the position of a lying person using a novel textile pressure sensor," *Sensors*, vol. 21, no. 1, p. 206, Dec. 2020.

[26] M. Hopkins, R. Vaidyanathan, and A. H. Mcgregor, "Examination of the performance characteristics of velostat as an in-socket pressure sensor," *IEEE Sensors J.*, vol. 20, no. 13, pp. 6992–7000, Jul. 2020.

[27] J. Niu, C. Zhang, X. Chen, C. Ma, L. Chen, and C. Tong, "A novel helmet fitness evaluation device based on the flexible pressure sensor matrix," *Sensors*, vol. 19, no. 18, p. 3823, Sep. 2019.

[28] Z. D. Prete, L. Monteleone, and R. Steindler, "A novel pressure array sensor based on contact resistance variation: Metrological properties," *Rev. Sci. Instrum.*, vol. 72, no. 2, pp. 1548–1553, Feb. 2001.

[29] J. A. Hidalgo-López, Ó. Oballe-Peinado, J. Castellanos-Ramos, J. A. Sánchez-Durán, R. Fernández-Ramos, and F. Vidal-Verdú, "High-accuracy readout electronics for piezoresistive tactile sensors," *Sensors*, vol. 17, no. 11, p. 2513, Nov. 2017.

[30] J. M. Gandarias, A. J. Garcia-Cerezo, and J. M. Gomez-de-Gabriel, "CNN-based methods for object recognition with high-resolution tactile sensors," *IEEE Sensors J.*, vol. 19, no. 16, pp. 6872–6882, Aug. 2019.

[31] I. Vehec and L. Livovsky, "Flexible resistive sensor based on velostat," in *Proc. 43rd Int. Spring Seminar Electron. Technol. (ISSE)*, May 2020, pp. 1–6.

[32] A. Dzedzickis *et al.*, "Polyethylene-carbon composite (Velostat) based tactile sensor," *Polymers*, vol. 12, no. 12, p. 2905, Dec. 2020.

[33] M. J. Edmonds, "Learning complex functional manipulations by human demonstration and fluent discovery," M.S. thesis, Dept. of Comp. Sci., UCLA, Los Angeles, CA, USA, 2017.

[34] S. Chen, M. Li, Y. Huang, H. Xu, G. Gu, and X. Guo, "Matrix-addressed flexible capacitive pressure sensor with suppressed crosstalk for artificial electronic skin," *IEEE Trans. Electron Devices*, vol. 67, no. 7, pp. 2940–2944, Jul. 2020.

[35] A. Tihak and D. Boskovic, "Experimental evaluation of challenges in designing a resistive pressure sensors," in *Proc. IEEE EUROCON 18th Int. Conf. Smart Technol.*, Jul. 2019, pp. 1–6.

[36] F. Castro, T. Pentiado, J. Blanco, R. Xavier, M. Sanches, and A. de Carvalho, "Crosstalk error analysis in IIDFC readout circuit for use in piezoresistive composite," *IEEE Sensors J.*, vol. 18, no. 1, pp. 382–389, Jan. 2018.

[37] B. Fan, S. Chen, J. Gao, and X. Guo, "Accurate recognition of light-weight objects with low resolution pressure sensor array," *IEEE Sensors J.*, vol. 20, no. 6, pp. 3280–3284, Mar. 2020.

[38] C. Medrano-Sanchez, R. Igual-Catalan, V. H. Rodriguez-Ontiveros, and I. Plaza-Garcia, "Circuit analysis of matrix-like resistor networks for eliminating crosstalk in pressure sensitive mats," *IEEE Sensors J.*, vol. 19, no. 18, pp. 8027–8036, Sep. 2019.

[39] J.-F. Wu, "Scanning approaches of 2-D resistive sensor arrays: A review," *IEEE Sensors J.*, vol. 17, no. 4, pp. 914–925, Feb. 2017.

[40] L. Shu, X. Tao, and D. D. Feng, "A new approach for readout of resistive sensor arrays for wearable electronic applications," *IEEE Sensors J.*, vol. 15, no. 1, pp. 442–452, Jan. 2015.

[41] S. S. Suprapto, A. W. Setiawan, H. Zakaria, W. Adiprawita, and B. Supartono, "Low-cost pressure sensor matrix using velostat," in *Proc. 5th Int. Conf. Instrum., Commun., Inf. Technol., Biomed. Eng. (ICICI-BME)*, Nov. 2017, pp. 137–140.

[42] C. Sun, W. Li, and W. Chen, "A compressed sensing based method for reducing the sampling time of a high resolution pressure sensor array system," *Sensors*, vol. 17, no. 8, p. 1848, Aug. 2017.

[43] S. Koh, B. Cho, J.-K. Park, C.-H. Kim, and S. Lee, "A fundamental experiment on contact position estimation on vision based dome-type soft tactile sensor using ready-made medium," in *Proc. 13th Int. Conf. Sens. Technol. (ICST)*, 2019, pp. 1–5.

[44] V. Chhoeum, Y. Kim, and S. D. Min, "A convolution neural network approach to access knee joint angle using foot pressure mapping images: A preliminary investigation," *IEEE Sensors J.*, vol. 21, no. 15, pp. 16937–16944, Aug. 2021.

[45] O. Ozioko, W. T. Navaraj, N. Yogeswaran, M. Hersh, and R. Dahiya, "Tactile communication system for the interaction between deafblind and robots," in *Proc. 27th IEEE Int. Symp. Robot Hum. Interact. Commun. (RO-MAN)*, Aug. 2018, pp. 416–421.

[46] S. Stassi, V. Cauda, G. Canavese, and C. F. Pirri, "Flexible tactile sensing based on piezoresistive composites: A review," *Sensors*, vol. 14, no. 3, pp. 5296–5332, 2014.

[47] X.-W. Zhang, Y. Pan, Q. Zheng, and X.-S. Yi, "Time dependence of piezoresistance for the conductor-filled polymer composites," *J. Polym. Sci. B, Polym. Phys.*, vol. 38, no. 21, pp. 2739–2749, Nov. 2000.

[48] X. Zhang and X. Ye, "Zero potential method measurement error analysis for networked resistive sensor arrays," *IET Sci., Meas. Technol.*, vol. 11, no. 3, pp. 235–240, May 2017.

[49] A. Krizhevsky, I. Sutskever, and G. E. Hinton, "ImageNet classification with deep convolutional neural networks," in *Proc. Adv. Neural Inf. Process. Syst. (NIPS)*, vol. 25, Dec. 2012, pp. 1097–1105.

[50] K. Simonyan and A. Zisserman, "Very deep convolutional networks for large-scale image recognition," 2014, *arXiv:1409.1556*.

[51] K. He, X. Zhang, S. Ren, and J. Sun, "Deep residual learning for image recognition," in *Proc. IEEE Conf. Comput. Vis. Pattern Recognit. (CVPR)*, Jun. 2016, pp. 770–778.

[52] A. Drimus, G. Kootstra, A. Bilberg, and D. Kragic, "Design of a flexible tactile sensor for classification of rigid and deformable objects," *Robot. Auton. Syst.*, vol. 62, no. 1, pp. 3–15, Jan. 2014.

[53] A. Shibata, A. Ikegami, M. Nakauma, and M. Higashimori, "Convolutional neural network based estimation of gel-like food texture by a robotic sensing system," *Robotics*, vol. 6, no. 4, p. 37, Dec. 2017.

[54] F. Pastor, J. M. Gandarias, A. J. García-Cerezo, and J. M. Gómez-de-Gabriel, "Using 3D convolutional neural networks for tactile object recognition with robotic palpation," *Sensors*, vol. 19, no. 24, p. 5356, Dec. 2019.

[55] F. B. Naeini *et al.*, "A novel dynamic-vision-based approach for tactile sensing applications," *IEEE Trans. Instrum. Meas.*, vol. 69, no. 5, pp. 1881–1893, May 2020.

[56] Z. Deng, Y. Jonetzko, L. Zhang, and J. Zhang, "Grasping force control of multi-fingered robotic hands through tactile sensing for object stabilization," *Sensors*, vol. 20, no. 4, p. 1050, Feb. 2020.

[57] L. Yuan and J. Li, "Smart cushion based on pressure sensor array for human sitting posture recognition," in *Proc. IEEE Sensors*, 2021.

Liangqi Yuan (Student Member, IEEE) received the B.E. degree in photo-electronic information science and engineering from the Beijing Information Science & Technology University, Beijing, China, in 2020. He is currently pursuing the M.S. degree in electrical and computer engineering with the Department of Electrical and Computer Engineering, Oakland University, Rochester, MI, USA. He is currently a Graduate Research Assistant under the supervision of Dr. Jia Li. His research interests are in the areas of sensors, the Internet of Things, human–computer interaction, signal processing, and machine learning.

Hongwei Qu (Member, IEEE) received the B.S. and M.S. degrees from Tianjin University, Tianjin, China, in 1988 and 1993, respectively, and the Ph.D. degree in electrical engineering from the University of Florida in 2006. He is currently a Professor at the Electrical and Computer Engineering Department, Oakland University, Rochester, MI, USA. Prior to his career in the USA, he had been a Faculty Member at Tianjin University for several years. Dr. Qu has been conducting research in solid-state devices and applications, micro-electro-mechanical systems (MEMS), and electronic materials, with nearly 100 publications in these areas. His main contributions include CMOS-MEMS integration and applications of various sensors in healthcare, of which he holds two patents. His research has been sponsored by federal and state agencies, as well as a number of industrial companies.

Jia Li (Senior Member, IEEE) received the B.S. degree in electronics and information systems from Peking University, Beijing, China, in 1996, and the M.S.E. and Ph.D. degrees in electrical engineering from the University of Michigan, Ann Arbor, MI, USA, in 1997 and 2002, respectively. She has been a Faculty Member with the School of Engineering and Computer Science, Oakland University, since 2002. She has authored/coauthored over 70 referred publications, including one book. Her research interests are in the areas of statistical learning and signal processing with applications in radar, sensor fusion, communications, and biomedical imaging. Her past and current research are sponsored by NSF, NIH, General Motors, Fiat Chrysler, the National Research Council, and Air Force Office of Scientific Research. Dr. Li serves as a member of technical committees of several international conferences and workshops.